Chem

CellPress

Article

Vanadium Oxide Pillared by Interlayer Mg^{2+} Ions and Water as Ultralong-Life Cathodes for Magnesium-Ion Batteries

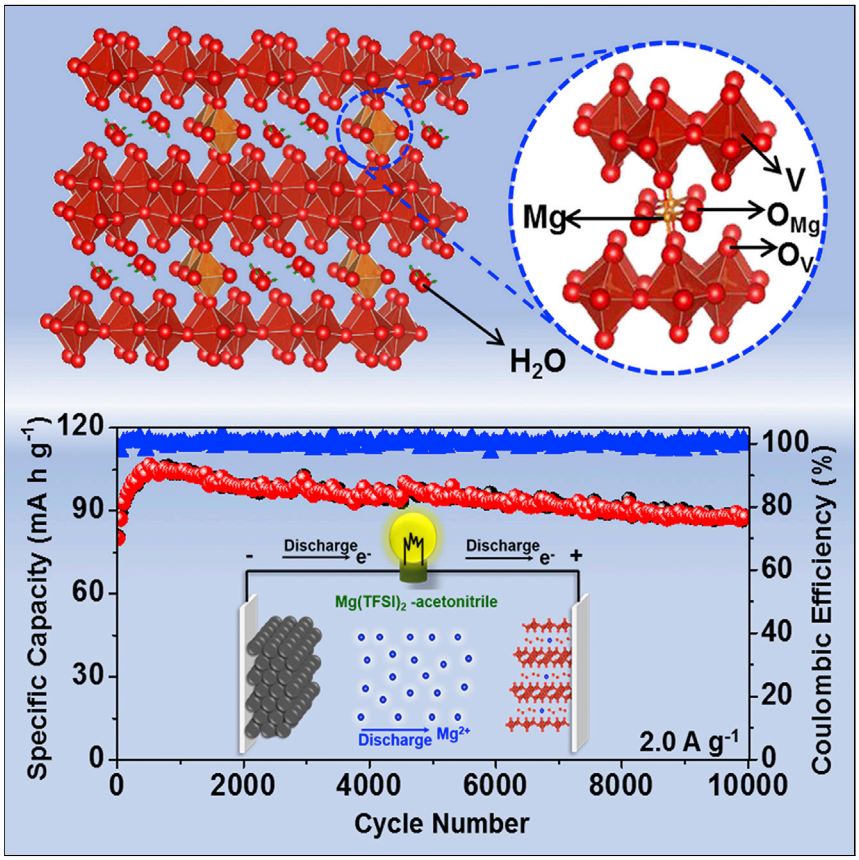

Yanan Xu, Xuanwei Deng, Qidong Li, ..., Jiantao Li, Qinyou An, Liqiang Mai

mlq518@whut.edu.cn

HIGHLIGHTS

Bilayer structured $Mg_{0.3}V_2O_5{\cdot}1.1H_2O$ was developed via chemical modification of α-V_2O_5

High voltage, high rates, and ultralong life for a MIB cathode

The pre-inserted Mg^{2+} and water endow good structural stability and fast Mg^{2+} diffusion

Mg-ion batteries are expected to be the next generation of energy storage technologies because of the significant advantages of low cost, good safety, and high performance. However, the biggest challenge is the lack of suitable Mg-insertion cathodes. Here, Mai and coworkers have designed a cathode with excellent rate capability and cycle stability for Mg-ion batteries. They reveal the Mg insertion mechanism within the bilayer-structured $Mg_{0.3}V_2O_5{\cdot}1.1H_2O$ in depth, illustrating the important application value of $Mg_{0.3}V_2O_5{\cdot}1.1H_2O$ for Mg-ion batteries.

Xu et al., Chem 5, 1–16
May 9, 2019
https://doi.org/10.1016/j.chempr.2019.02.014

Please cite this article in press as: Xu et al., Vanadium Oxide Pillared by Interlayer Mg^{2+} Ions and Water as Ultralong-Life Cathodes for Magnesium-Ion Batteries, Chem (2019), https://doi.org/10.1016/j.chempr.2019.02.014

Chem

CellPress

Article

Vanadium Oxide Pillared by Interlayer Mg^{2+} Ions and Water as Ultralong-Life Cathodes for Magnesium-Ion Batteries

Yanan Xu,[1] Xuanwei Deng,[1] Qidong Li,[1,2] Guobin Zhang,[1] Fangyu Xiong,[1] Shuangshuang Tan,[1] Qiulong Wei,[1,3] Jun Lu,[2] Jiantao Li,[1] Qinyou An,[1] and Liqiang Mai[1,4,*]

SUMMARY

Magnesium-ion batteries (MIBs) show great potential for large-scale energy storage because of the advantages of low cost and safety, but their application is severely hindered by the difficulty in finding desirable electrode materials. Herein, we develop a bilayer-structured vanadium oxide ($Mg_{0.3}V_2O_5 \cdot 1.1H_2O$) with synergistic effect of Mg^{2+} ions and lattice water as the cathode material for MIBs. The pre-intercalated Mg^{2+} ions provide high electronic conductivity and excellent structural stability. The lattice water enables fast Mg^{2+} ions mobility because of its charge shielding effect. As a result, the $Mg_{0.3}V_2O_5 \cdot 1.1H_2O$ exhibits excellent rate performance and an unprecedented cycling life with capacity retention of 80.0% after 10,000 cycles. In addition, the $Mg_{0.3}V_2O_5 \cdot 1.1H_2O$ exhibits good electrochemical performance in full MIBs. This scalable Mg^{2+} host material is a promising candidate as a cathode for MIBs, and its high performance is expected to meet the requirements for large-scale storage applications.

INTRODUCTION

Lithium-ion batteries (LIBs) have become indispensable in our daily lives, with applications ranging from portable electronic devices to electric vehicles.[1] However, their further development and applications are being limited by the high cost of lithium (Li) and safety issues.[2–4] Multivalent intercalation batteries are highly promising substitutes benefitting from the advantages of good safety, low cost, and high energy density.[4,5] Among them, magnesium (Mg) batteries have been regarded as the most promising candidate.[6–11] In 2000, Aurbach et al., in pioneering work, achieved a significant breakthrough in the development of rechargeable Mg batteries.[12] However, the low operating voltage and low reversible specific capacity of the Chevrel phase Mo_6S_8 limited the performance of the rechargeable Mg battery. Since then, studies on Mg batteries have focused on searching for more desirable Mg intercalation cathodes. But unlike insertion of monovalent Li^+ and Na^+, insertion of bivalent Mg^{2+} in the host materials is more difficult.[13,14] This is because of the strong interaction between the host lattice and Mg^{2+}, which results in sluggish solid-state diffusion and large potential polarization.[13,14] Thus, the ideal crystal structure must possess a more coordinated environment for Mg diffusion with lower migration barriers.[15,16]

Many electrode materials, including transition-metal sulfides,[17–20] transition-metal oxides,[14,16,21–27] and polyanionic compounds,[28,29] have been investigated for Mg-ion batteries (MIBs). Among them, oxide cathodes show great potential because

The Bigger Picture

Presently, energy storage technologies are gaining prominence in our society. Lithium-ion batteries (LIBs) in particular have been widely used in our daily lives. However, the high cost and safety issues surrounding lithium are impediments to their further usage. Recently, a series of new-type energy storage batteries have attracted significant attention. Among them, magnesium-ion batteries (MIBs) are regarded as one of the most promising candidates because of the abundant Mg resource, low cost, and good safety. However, up until now, it remains challenging to discover and develop suitable electrode materials because of the sluggish solid-state diffusion of Mg^{2+}. Here, we report a bilayer-structured vanadium oxide—$Mg_{0.3}V_2O_5 \cdot 1.1H_2O$—that shows remarkable reversibility of Mg^{2+} insertion and reveals the accompanying chemical insertion mechanisms. Our work aims at bringing new insights to developing high-performance, low-cost, and extremely safe MIB cathodes needed for large-scale storage applications.

transition-metal ions can change by two or more oxidation states, which makes it easy to achieve local electroneutrality and lower barriers to Mg^{2+} diffusion.[7] Recently, bilayer-structured $V_2O_5 \cdot nH_2O$ materials have attracted more attention as a potential MIB cathode.[24,25,30–33] Thanks to the "shielding effect" of water, the cations can be easily inserted into the host materials.[34,35] However, the rate capability and cycle life of these xerogel materials remain insufficient to meet the ever-increasing energy demand. The inferior rate capability and cycle life could be due to the following reasons: (1) poor electrical conductivity causing greater polarization; (2) water ejection from the crystal structure, leading to an undesirable side reaction with the Mg anode; and (3) poor structural stability resulting from larger interlamellar spacing due to excess water between layers. It is worth noting that pre-intercalated metal ions ($M_xV_2O_5$, M = metal ion) have been reported to significantly increase the structural stability and electronic conductivity of layered vanadium oxides in different battery systems.[36–38] Thus, taking all these into consideration, developing cathode materials with fast Mg^{2+} ions mobility and stable structure to obtain good cycle life is of significant importance in practice.

Herein, we report a Mg^{2+} pre-intercalated hydrated vanadium oxide, $Mg_{0.3}V_2O_5 \cdot 1.1H_2O$, to tackle the above-mentioned limitations. The intercalated Mg^{2+} works collaboratively with structural water to provide high electronic conductivity, fast ion mobility, and good structural stability during cycling. As a Mg intercalation cathode, the $Mg_{0.3}V_2O_5 \cdot 1.1H_2O$ shows unprecedented electrochemical performance: an ultralong cycling life with capacity retention of 80.0% after 10,000 cycles at a high current density of 2 A g^{-1}, which is superior to common cathode materials for LIBs and sodium-ion batteries (SIBs) in terms of performance. A single-nanowire device directly shows good electrical conductivity of the obtained materials. *In situ* X-ray diffraction (XRD) analysis, X-ray absorption near-edge spectroscopy (XANES), and solid-state nuclear magnetic resonance (NMR) spectroscopy are used to elucidate the structure and reaction mechanism of the material, providing bases for understanding the remarkable performance. Moreover, $Mg_{0.3}V_2O_5 \cdot 1.1H_2O$ exhibits good electrochemical performance in full MIBs.

RESULTS

Formation Mechanism of the Bilayer-Structured $Mg_{0.3}V_2O_5 \cdot 1.1H_2O$

The $Mg_{0.3}V_2O_5 \cdot 1.1H_2O$ nanowires were synthesized via chemical modification of α-V_2O_5. In brief, V_2O_5 and $C_4H_6O_4Mg \cdot 4H_2O$ as raw materials were dissolved in deionized water. H_2O_2 was chosen as the reducing agent. Then, the homogeneous solution was put into a 50 mL Teflon vessel and heated at 200°C for 48 h to finally yield the $Mg_{0.3}V_2O_5 \cdot 1.1H_2O$ nanowires. Schematic diagrams of the formation of the bilayer-structured $Mg_{0.3}V_2O_5 \cdot 1.1H_2O$ are shown in Figure 1. First, H_2O_2 lowers the valence state of V in α-V_2O_5, resulting in the transformation of VO_5 square pyramids to VO_6 octahedra. As a result, the crystal structure is rearranged, and a large number of water molecules are embedded into the interlayer. A bilayered structure with a larger interlayer space is then formed, which provides spacious channels for subsequent insertion of Mg ions. The insertion of Mg ions into the layers leads to layer slippage and shrinkage as a result of the coordination between Mg^{2+} and lattice oxygen. Finally, driven by the thermodynamic energy, the bilayer-structured $Mg_{0.3}V_2O_5 \cdot 1.1H_2O$ is formed. In addition, we prepared $V_2O_5 \cdot nH_2O$ and $Mg_{0.3}V_2O_5$ nanowires to investigate the roles of Mg^{2+} ions and lattice water. The $V_2O_5 \cdot nH_2O$ nanowires were prepared via the same process as $Mg_{0.3}V_2O_5 \cdot 1.1H_2O$ but without $C_4H_6O_4Mg \cdot 4H_2O$, whereas $Mg_{0.3}V_2O_5$ was obtained by annealing $Mg_{0.3}V_2O_5 \cdot 1.1H_2O$ at 400°C for 2 h in Ar with a heating rate of 2°C min^{-1}.

[1]State Key Laboratory of Advanced Technology for Materials Synthesis and Processing, International School of Materials Science and Engineering, Wuhan University of Technology, Wuhan, Hubei 430070, P.R. China

[2]Chemical Sciences and Engineering Division, Argonne National Laboratory, Argonne, IL 60439, USA

[3]Department of Materials Science and Engineering, University of California, Los Angeles, Los Angeles, CA 90095-1595, USA

[4]Lead Contact

*Correspondence: mlq518@whut.edu.cn

https://doi.org/10.1016/j.chempr.2019.02.014

Please cite this article in press as: Xu et al., Vanadium Oxide Pillared by Interlayer Mg^{2+} Ions and Water as Ultralong-Life Cathodes for Magnesium-Ion Batteries, Chem (2019), https://doi.org/10.1016/j.chempr.2019.02.014

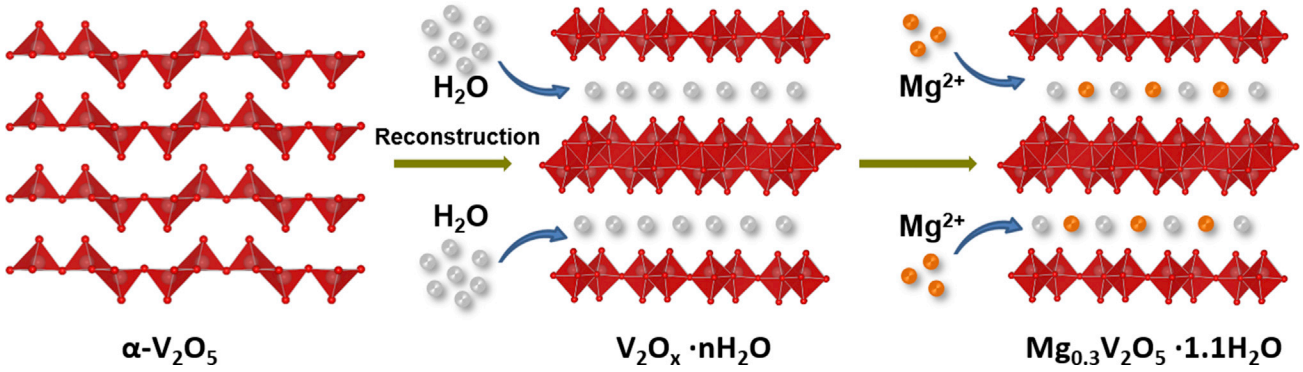

Figure 1. Schematic Diagrams of the Formation of the Bilayer-Structured $Mg_{0.3}V_2O_5 \cdot 1.1H_2O$

Structure and Morphology of Characterization $Mg_{0.3}V_2O_5 \cdot 1.1H_2O$

The XRD pattern of $Mg_{0.3}V_2O_5 \cdot 1.1H_2O$ is shown in Figure 2A. Clearly, $Mg_{0.3}V_2O_5 \cdot 1.1H_2O$ shows sharp diffraction peaks and displays lamellar ordering as dominated by the pronounced (001) reflections. The four standard diffraction peaks without any impurity prove the single-phase nature of the xerogel material. The interlayer spacing is about 11.9 Å. The XRD pattern of $V_2O_5 \cdot nH_2O$ is similar to that of $Mg_{0.3}V_2O_5 \cdot 1.1H_2O$ with lower crystallinity (Figure S1). Meanwhile, without Mg^{2+} intercalation, the 001 peak shifts to a lower degree, indicating a larger interlayer spacing. This means that Mg^{2+} ions are inserted in between the V_2O_5 bilayers. A schematic diagram of the crystal structure of $Mg_{0.3}V_2O_5 \cdot 1.1H_2O$ is shown in Figure 2B. It can be seen that each V_2O_5 layer is composed of VO_6 octahedra and VO_5 square pyramids, extending infinitely in the a–b plane. The ordered MgO_6 octahedra act as pillars in the interlayer of two V_2O_5 bilayers to maintain the structural stability. The water exists in the non-embedded sites with stable hydrogen-bonded arrangements in the *a* and *b* directions, which can accommodate additional Mg^{2+} in the discharge process. The crystal structure of $Mg_{0.3}V_2O_5 \cdot 1.1H_2O$ is similar to that of $Zn_{0.25}V_2O_5 \cdot nH_2O$.[37] With regard to the $Mg_{0.3}V_2O_5$, the bilayer structure is not obtained after the removal of the lattice water (Figure S1). Without the structural support of water, the reduced lattice space is detrimental to Mg ions transport, leading to a foreseeable reduction in electrochemical performance.

Inductively coupled plasma optical emission spectroscopy analysis (ICP-OES) and thermogravimetric analysis (TGA) were used to investigate the chemical composition of the obtained xerogel material, as shown in Table S1 and Figure S2. The calculated molecular formula was determined to be $Mg_{0.3}V_2O_5 \cdot 1.1H_2O$, and the average valence of vanadium is $V^{4.7+}$. The X-ray photoelectron spectrum (XPS) was used to further investigate the composition of the $Mg_{0.3}V_2O_5 \cdot 1.1H_2O$ electrode as well as the valence state of the vanadium ion. As shown in Figure S3A, Mg, V, and O elements were detected in the survey spectrum, which is consistent with the ICP-OES analysis. The two peaks (Figure S3B) located at 517.3 and 524.5 eV correspond to the $V2p_{3/2}$ and $V2p_{1/2}$ of V^{5+}, respectively.[37] Carefully analyzing the V high-resolution spectra, we found the existence of an overlapping peak located at 516.0 eV with less intensity, which illustrates the presence of a certain amount of V^{4+} in our samples. The V^{4+}/V^{5+} ratio was around 37%, suggesting that Mg ions intercalate into the interlayers and coordinate with the lattice oxygen to reduce the valence of vanadium.

We performed scanning electron microscopy (SEM) and transmission electron microscopy (TEM) to study the morphological structure of the three samples. The

Please cite this article in press as: Xu et al., Vanadium Oxide Pillared by Interlayer Mg^{2+} Ions and Water as Ultralong-Life Cathodes for Magnesium-Ion Batteries, Chem (2019), https://doi.org/10.1016/j.chempr.2019.02.014

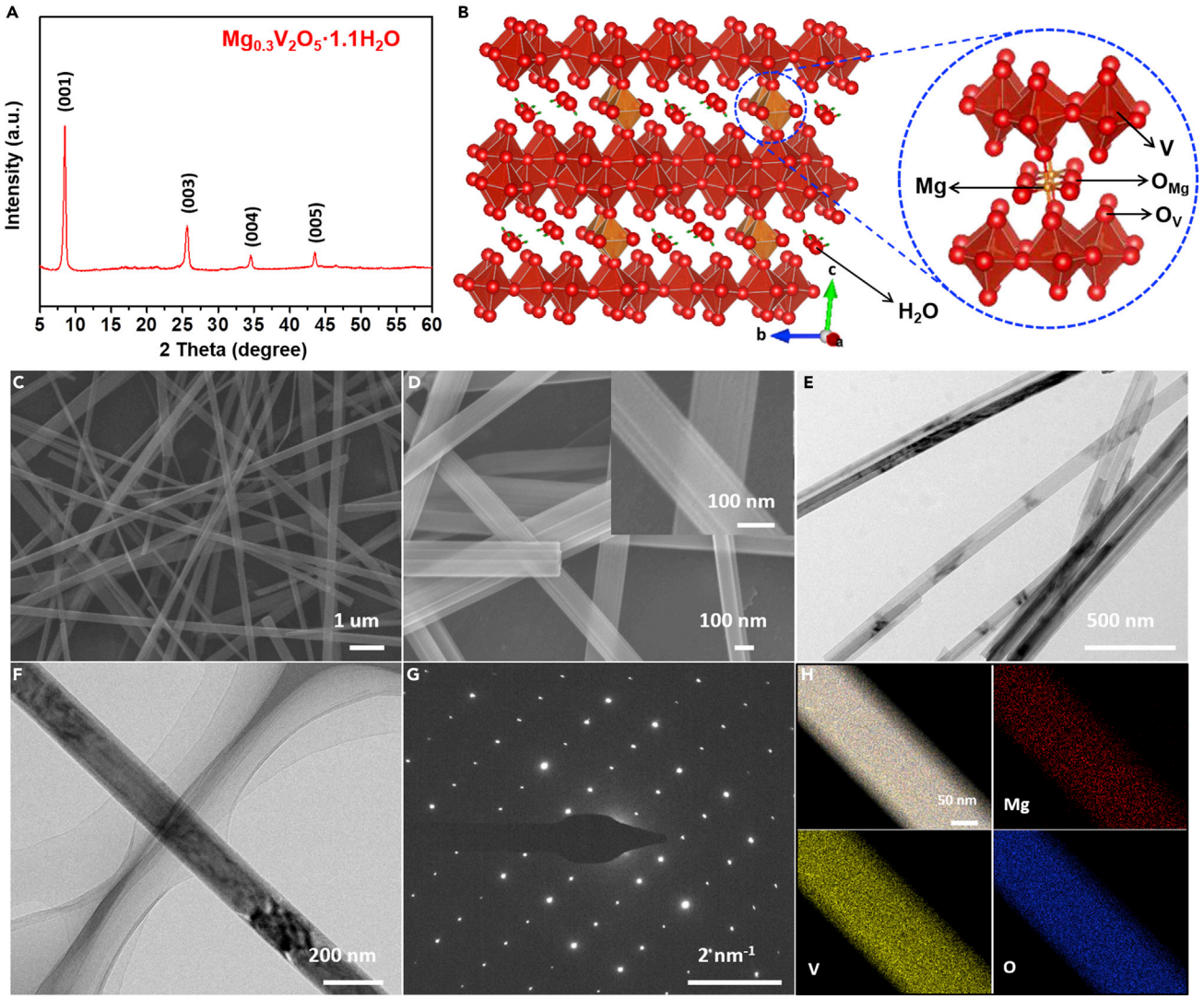

Figure 2. Structure and Morphology of the $Mg_{0.3}V_2O_5{\cdot}1.1H_2O$

(A) XRD diffraction pattern of $Mg_{0.3}V_2O_5{\cdot}1.1H_2O$ nanowires.

(B) Schematic diagram of the crystal structure of $Mg_{0.3}V_2O_5{\cdot}1.1H_2O$.

(C–H) FESEM images (C and D), TEM images (E and F), SAED pattern (G), and TEM-EDX element mapping images (H) of $Mg_{0.3}V_2O_5{\cdot}1.1H_2O$ nanowires.

SEM images (Figures 2C and 2D) show that $Mg_{0.3}V_2O_5{\cdot}1.1H_2O$ possesses uniform nanowire morphology characteristics with a smooth and clean surface. The lengths of the nanowires are about a dozen micrometers with an average diameter of 100–150 nm. This one-dimensional (1D) nanostructure is beneficial to shorten the Mg^{2+} diffusion length. We performed TEM characterizations to further investigate the morphology and structure of $Mg_{0.3}V_2O_5{\cdot}1.1H_2O$. As shown in Figures 2E and 2F, a threadlike morphology with a clean surface could be clearly observed. The diameter was about 150 nm, which is consistent with the SEM images. Figure 2G shows the selected area electron diffraction (SAED) image of $Mg_{0.3}V_2O_5{\cdot}1.1H_2O$. The uniform and well-ordered space lattices suggest the single-crystal diffraction pattern. The elemental mappings show the existence and uniform distribution of Mg, V, and O in $Mg_{0.3}V_2O_5{\cdot}1.1H_2O$ (Figure 2H). We applied energy-dispersive X-ray spectroscopy (EDX) analysis to verify the elemental content as shown in Figure S4. The result was highly consistent with that of

Please cite this article in press as: Xu et al., Vanadium Oxide Pillared by Interlayer Mg^{2+} Ions and Water as Ultralong-Life Cathodes for Magnesium-Ion Batteries, Chem (2019), https://doi.org/10.1016/j.chempr.2019.02.014

ICP-OES analysis. For $V_2O_5 \cdot nH_2O$, the morphology was similar to that of $Mg_{0.3}V_2O_5 \cdot 1.1H_2O$ with single-crystal characteristics (Figure S5). However, for $Mg_{0.3}V_2O_5$, the SEM image (Figure S6A) shows that the nanowires aggregated together with severe breakages after the high temperature treatment, which is not conducive to Mg^{2+} ions diffusion. The lengths of the nanowires are only several micrometers with an average diameter of 150 nm. TEM images (Figures S6B and S6C) reveal that the surface of the nanowires was no longer smooth, and some pore structures formed between the nanowires. The SAED image (Figure S6D) shows the single-crystal diffraction pattern. Figure S7 shows the Brunauer-Emmerr-Teller (BET) surface area of the three samples. The BET surface area of $Mg_{0.3}V_2O_5 \cdot 1.1H_2O$ was measured to be 38.23 $m^2\ g^{-1}$, higher than that of $V_2O_5 \cdot nH_2O$ (33.91 $m^2\ g^{-1}$) and $Mg_{0.3}V_2O_5$ (28.76 $m^2\ g^{-1}$). The larger BET surface area of the $Mg_{0.3}V_2O_5 \cdot 1.1H_2O$ would be beneficial for electrolyte penetration and ion transfer.

Mg-Ion Storage Performance of the $Mg_{0.3}V_2O_5 \cdot 1.1H_2O$ Cathode

To investigate the electrochemical performances of the prepared samples, we used coin cells for the electrochemical performance test with 0.3 M $Mg[N(SO_2CF_3)_2]_2$ ($Mg(TFSI)_2$) in acetonitrile (AN) as electrolyte and activated carbon (AC) cloth as the anode. $Mg(TFSI)_2$ electrolyte has been demonstrated to be highly compatibile with most cathodes and have high oxidation stability and high ionic conductivity.[7,39] The Mg metal anode will form a passive film in the $Mg(TFSI)_2$/AN electrolyte, which does not allow the Mg ion to pass through.[39] Hence, AC was chosen as the anode because of its high surface area, which ensures adequate charge storage via electrical double-layer capacitance to guarantee full charge balance in the process of Mg intercalation.[5,7,26,27] The potential of the AC electrode was calculated as 2.4 V versus Mg^{2+}/Mg.[5,26]

The charge and discharge curves of the three samples at 0.1 A g^{-1} in 1.4–3.4 V (versus Mg^{2+}/Mg) are shown in Figure 3A. $Mg_{0.3}V_2O_5 \cdot 1.1H_2O$ possessed three discharge voltage plateaus at around 3.02, 2.25, and 1.40 V (versus Mg^{2+}/Mg), which can be ascribed to the multistep Mg^{2+} intercalation behaviors in the bilayer structure. The discharge capacity of $Mg_{0.3}V_2O_5 \cdot 1.1H_2O$ reached 164 mA h g^{-1}, corresponding to 0.5 Mg^{2+} ions per formula unit insertion into $Mg_{0.3}V_2O_5 \cdot 1.1H_2O$. The charge-discharge curve of $V_2O_5 \cdot nH_2O$ was similar to that of $Mg_{0.3}V_2O_5 \cdot 1.1H_2O$ with a lower discharge capacity of 114 mA h g^{-1}. But for $Mg_{0.3}V_2O_5$, no obvious plateaus were observed, and the lowest discharge capacity was 91 mA h g^{-1}. Figure S8 shows the cyclic voltammetry (CV) of the three samples at a scan rate of 0.1 mV s^{-1} between 1.4 and 3.4 V versus Mg^{2+}/Mg. Clearly, the results are consistent with the charge-discharge curves. The much higher current and complete repetition in the initial two cycles of $Mg_{0.3}V_2O_5 \cdot 1.1H_2O$ indicate its faster kinetics and higher reversibility during Mg^{2+} intercalation and deintercalation. The cycling performance of the three samples at a low current density of 0.1 A g^{-1} is shown in Figure 3B. The initial discharge capacity of $Mg_{0.3}V_2O_5 \cdot 1.1H_2O$ was 164 mA h g^{-1}, and after 500 cycles the capacity was perfectly maintained with a Coulombic efficiency of nearly 100%, which shows high reversible capacity and excellent cycle stability compared with that of $V_2O_5 \cdot nH_2O$ and $Mg_{0.3}V_2O_5$ at low current density. Rate performances are shown in Figure 3C. $Mg_{0.3}V_2O_5 \cdot 1.1H_2O$ delivered high capacities of 162, 145, 134, 120, 85, and 50 mA h g^{-1} at current densities of 0.1, 0.2, 0.5, 1.0, 2.0, and 4.0 A g^{-1}, respectively. When the rate was turned back to 0.1 A g^{-1}, it showed good capacity recoverability, whereas $V_2O_5 \cdot nH_2O$ and $Mg_{0.3}V_2O_5$ electrodes exhibited lower and unstable specific capacities at low current densities and suffered a rapid capacity decay at increased current densities. Figure 3D shows the discharge-charge curves of $Mg_{0.3}V_2O_5 \cdot 1.1H_2O$ at different current densities. Even

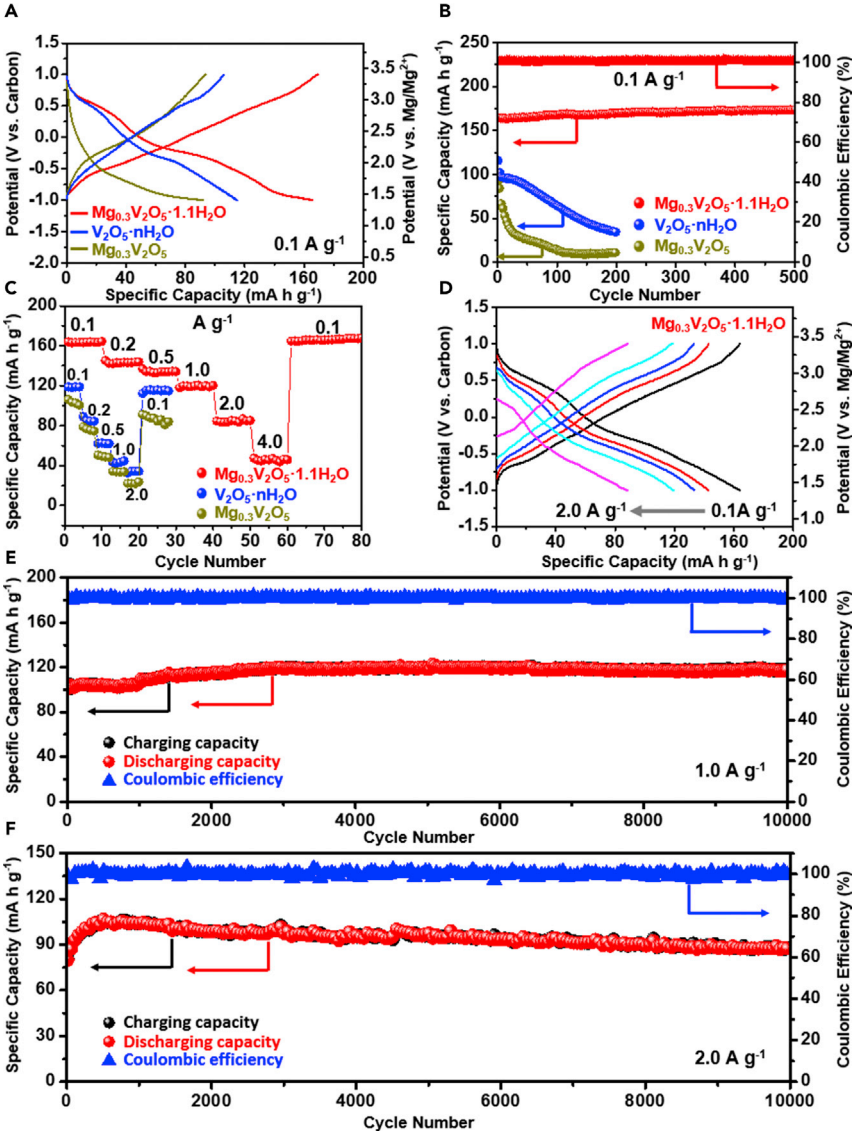

Figure 3. Electrochemical Performance of the $Mg_{0.3}V_2O_5 \cdot 1.1H_2O$, $V_2O_5 \cdot nH_2O$, and $Mg_{0.3}V_2O_5$ Electrodes

(A–C) Charge-discharge curves (A), cycling performances (B), and rate performances (C) of $Mg_{0.3}V_2O_5 \cdot 1.1H_2O$, $V_2O_5 \cdot nH_2O$, and $Mg_{0.3}V_2O_5$.

(D) Charge-discharge curves of $Mg_{0.3}V_2O_5 \cdot 1.1H_2O$ at different rates.

(E and F) Ultralong cycling life of $Mg_{0.3}V_2O_5 \cdot 1.1H_2O$ for 10,000 cycles at 1 A g^{-1} (E) and 2 A g^{-1} (F).

at high current densities, the $Mg_{0.3}V_2O_5 \cdot 1.1H_2O$ showed good electrochemical behavior.

The cycle life at different current densities was further investigated. Figure S9 shows the discharge-charge curves and cycling performances of $Mg_{0.3}V_2O_5 \cdot 1.1H_2O$ at 0.2 and 0.5 A g^{-1}, respectively. After 500 and 3,000 cycles, the capacity does not decay with almost 100% Coulombic efficiency. Ultralong-life cycling performance of $Mg_{0.3}V_2O_5 \cdot 1.1H_2O$ at a high current density of 1 A g^{-1} is shown in Figure 3E. The initial discharge capacity is 108 mA h g^{-1}. After 10,000 cycles, the capacity is perfectly maintained. Even at 2 A g^{-1}, 80.0% of the maximum capacity is achieved

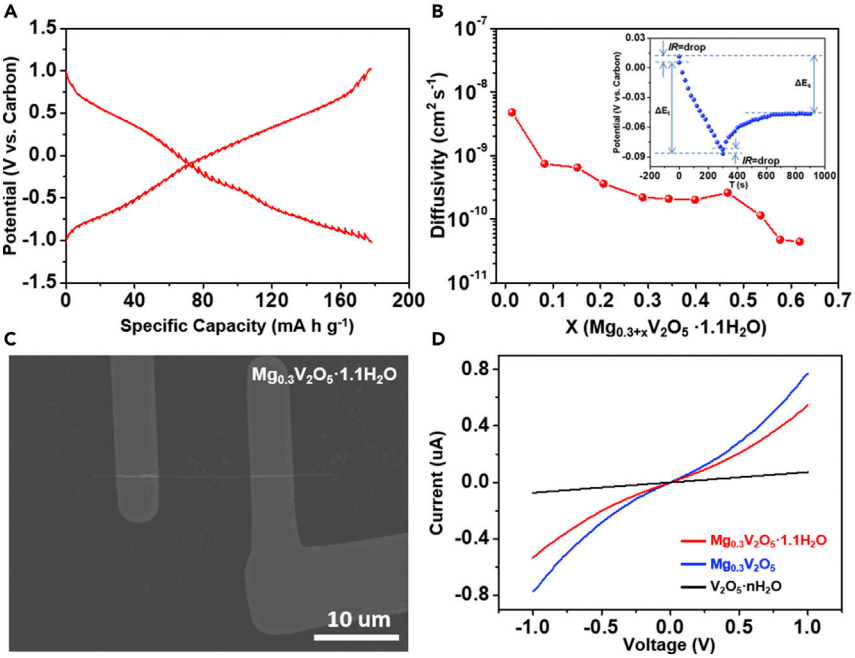

Figure 4. Kinetics Analysis of the Electrochemical Behavior toward Mg^{2+} for the $Mg_{0.3}V_2O_5 \cdot 1.1H_2O$ Electrode

(A) GITT curve of $Mg_{0.3}V_2O_5 \cdot 1.1H_2O$.

(B) Diffusivity versus state of discharge (inset: GITT potential response curve with time). The experiment was carried out at constant current pulse of 50 mA g^{-1} for 5 min, followed by a relaxation period of 10 min and a voltage range.

(C) SEM images of the $Mg_{0.3}V_2O_5 \cdot 1.1H_2O$ single-nanowire devices.

(D) *I-V* curves of the three samples.

after 10,000 cycles with a high average Coulombic efficiency of 99.91% (Figure 3F). The increase in capacity for the initial cycles could be attributed to the activation of bilayer $Mg_{0.3}V_2O_5 \cdot 1.1H_2O$. Here, it is worth mentioning that the $Mg_{0.3}V_2O_5 \cdot 1.1H_2O$ cathode material affords unprecedented cycling stabilities for MIBs. For $V_2O_5 \cdot nH_2O$, the lower electrical conductivity reduces the diffusion kinetics, leading to a greater polarization and rapid capacity decay during cycling (Figure S10A). With regard to $Mg_{0.3}V_2O_5$, without the water support, the lattice space shrinks severely and the "shielding effect" disappears, resulting in lower Mg^{2+} intercalation efficiency and Mg^{2+} diffusion rate. Finally, it shows low reversible capacity and fast capacity fading during charging and discharging (Figure S10B). Therefore, the synergistic effects of Mg^{2+} ions and lattice water play an important role in improving the electrochemical performance of $Mg_{0.3}V_2O_5 \cdot 1.1H_2O$.

Kinetics Analysis of $Mg_{0.3}V_2O_5 \cdot 1.1H_2O$ Cathode

In order to further investigate the kinetics of ion solid-state diffusion, we performed galvanostatic intermittent titration technique (GITT) of $Mg_{0.3}V_2O_5 \cdot 1.1H_2O$, as shown in Figure 4A. $Mg_{0.3}V_2O_5 \cdot 1.1H_2O$ delivered a reversible capacity of 176 mA h g^{-1} in the voltage window of 1.4 and 3.4 V versus Mg^{2+}/Mg, corresponding to a discharge product of $Mg_{0.3+x}V_2O_5 \cdot 1.1H_2O$ (x = 0.62). In addition, the diffusion coefficient D^{GITT} (cm^2 s^{-1}) can be calculated according to the following formula (Equation 1):[24]

$$D^{GITT} = \frac{4}{\pi\tau}\left(\frac{m_B V_M}{M_B S}\right)^2\left(\frac{\Delta E_s}{\Delta E_\tau}\right)^2, \qquad \text{(Equation 1)}$$

Please cite this article in press as: Xu et al., Vanadium Oxide Pillared by Interlayer Mg^{2+} Ions and Water as Ultralong-Life Cathodes for Magnesium-Ion Batteries, Chem (2019), https://doi.org/10.1016/j.chempr.2019.02.014

Where τ, m_B, V_M, M_B, and S are the constant current pulse time, mass, molar volume, molar mass, and electrode-electrolyte interface area of $Mg_{0.3}V_2O_5{\cdot}1.1H_2O$, respectively. ΔE_s is the voltage difference during the open circuit period, and ΔE_t represents the total change of cell voltage during a constant current pulse excluding the *IR* drop (inset of Figure 4B). From the calculated results (Figure 4B), even though the Mg^{2+} diffusivity decreases from 4.78×10^{-9} to 4.42×10^{-11} $cm^2\ s^{-1}$ as a result of the charge repulsion resulting from the increase in Mg^{2+} concentration in the host, it still indicates the fast charge-transfer kinetics. The high diffusion rate mainly originates from the lattice water, which can effectively shield the charge of Mg^{2+} and reduce interaction between host lattice and Mg^{2+},[34,35] resulting in good Mg^{2+} mobility and thus enhanced electrochemical performance. Moreover, we designed and assembled single-nanowire devices to test the electrical conductivity of the samples, as shown in Figures 4C and S11. Without the influence of conductive additives and binders, the intrinsic electrical conductivities of the samples were directly tested. After calculation, the electrical conductivities of $Mg_{0.3}V_2O_5{\cdot}1.1H_2O$, $Mg_{0.3}V_2O_5$, and $V_2O_5{\cdot}nH_2O$ were around 8.5×10^2, 5.0×10^3, and 10.1 S m^{-1}, respectively (Figure 4D), which indicates that the intercalation of Mg ions greatly improves the electrical conductivity of V_2O_5, guaranteeing fast electronic transmission in the Mg^{2+} intercalation process.

Mg-Storage Mechanism of $Mg_{0.3}V_2O_5{\cdot}1.1H_2O$

To investigate the crystal structure evolution of $Mg_{0.3}V_2O_5{\cdot}1.1H_2O$ during charging and discharging, we employed the *in-situ* XRD technique as shown in Figure 5A. During the discharging process, Mg^{2+} ions were gradually embedded in the cathode material. The main (001) diffraction peak (8.7°) shifted slightly toward a higher angle along with the reduction in crystallinity. Meanwhile, the (003) peak also shifted toward higher angle from 25.7° to 26.5°. Because of the smaller interplanar spacing of the (003) crystal plane, according to the Bragg equation, the shifting degree of the (003) diffraction peak was much bigger than that of the (001) peak. After full discharge, the interlayer spacing of bilayer $Mg_{0.3}V_2O_5{\cdot}1.1H_2O$ reduced from 11.9 to 11.4 Å. Such a small lattice change is a benefit of the pillaring effect of the pre-intercalated Mg^{2+} to maintain structural stability. The decrease in interlayer spacing is because the intercalated Mg^{2+} ions coordinate with the lattice oxygen, which causes the interlayer space to shrink.[40,41] In addition, there was no obvious new phase formation during the whole magnesiation process apart from the peak shift. During the subsequent charge process, Mg^{2+} ions were extracted from the interlayer, resulting in a full recovery of the interlayer spacing of the bilayer $Mg_{0.3}V_2O_5{\cdot}1.1H_2O$. The second discharge-charge process followed the same trajectory, demonstrating the high reaction reversibility in $Mg_{0.3}V_2O_5{\cdot}1.1H_2O$. The fully reversible and stable crystal structure of $Mg_{0.3}V_2O_5{\cdot}1.1H_2O$ during the intercalation and extraction of Mg^{2+} ions gives reason for the ultralong cycle stability. This was further demonstrated by the morphology and structure characterizations after the Mg^{2+}-ion insertion and extraction process, as shown in Figure S12. SEM and TEM images of the $Mg_{0.3}V_2O_5{\cdot}1.1H_2O$ electrode after 500 cycles (0.1 A g^{-1}) and 10,000 cycles (1 A g^{-1}) were collected (Figures S12A, S12B, S12D, and S12E) and show that the nanowire morphology was well preserved. Meanwhile, both of them maintained a relatively complete crystal structure after long cycling, as demonstrated by high-resolution TEM (HRTEM) images (insets of Figures S12B and S12E) and SAED patterns (Figures S12C and S12F), fully demonstrating the structural stability of $Mg_{0.3}V_2O_5{\cdot}1.1H_2O$. The above results show that the intercalated Mg^{2+} ions of $Mg_{0.3}V_2O_5{\cdot}1.1H_2O$ provide excellent structural stability, which endows remarkable Mg storage performance.

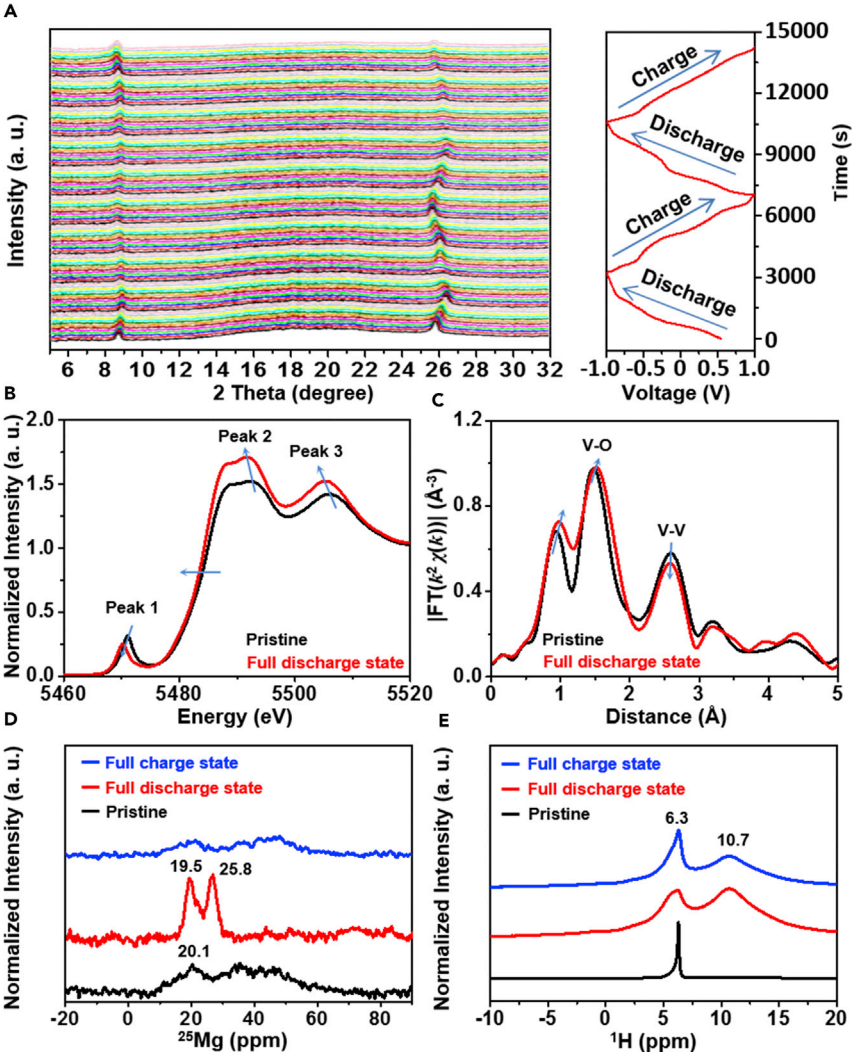

Figure 5. Mg-Storage Mechanism and Structure Characterizations of $Mg_{0.3}V_2O_5 \cdot 1.1H_2O$ after Magnesiation

(A) *In situ* XRD measurement of $Mg_{0.3}V_2O_5 \cdot 1.1H_2O$ during the first two electrochemical cycles showing the evolution of the XRD pattern as a function of intercalated Mg^{2+} concentration.
(B and C) Vanadium K-edge XANES spectra of pristine $Mg_{0.3}V_2O_5 \cdot 1.1H_2O$ (black line) and $Mg_{0.3}V_2O_5 \cdot 1.1H_2O$ after full discharging (red line) (B) and the corresponding FT-EXAFS spectra in R space (C).
(D and E) ^{25}Mg (D) and ^{1}H (E) MAS NMR spectra collected for pristine $Mg_{0.3}V_2O_5 \cdot 1.1H_2O$ (black line) and $Mg_{0.3}V_2O_5 \cdot 1.1H_2O$ after full discharging (red line) and full charging (blue line).

We performed vanadium XANES to elucidate the reaction mechanism and the fine structure of the material, as shown in Figure 5B. After magnesiation, the K-edge of the vanadium slightly shifts toward the lower binding energy, indicating a decrease in the average valence state of vanadium. In addition, the variations of pre-edge (peak 1) and the edge resonance (peak 2) also represent the change of valence state and chemical environment of the vanadium.[42] The pre-edge peak is located at 5,471 eV, and its intensity is in positive correlation with the deviation from the octahedral symmetry of the vanadium site.[43,44] The intensity of the pre-edge peak reduces and the peak position shifts to lower energy after Mg^{2+} insertion. The edge resonance corresponds to the energy absorption by core electrons. After

discharge, the intensity increases and the edge position shifts to lower energy, which is consistent with the pre-edge peak. Peak 3, seen in Figure 5B, is the first extended X-ray absorption spectroscopy oscillation,[43,45] and its position moves to lower energy after Mg^{2+} insertion, which is consistent with the V_2O_5 xerogel cathode.[43] To obtain the detailed bonding and coordination information of the vanadium site, we also recorded the corresponding Fourier transform extended X-ray absorption spectroscopy (FT-EXAFS) spectra as shown in Figure 5C. After magnesiation, Mg ions coordinate with oxygen atoms, and the length of V–O bond (at around 1.5 Å) slightly increases. Meanwhile, the length of V–V bond (at around 2.6 Å) marginally shortens. It should be noted that the V–O bonds form the skeleton of the crystal structure, and hence bond changes of V–O and V–V are closely related to structural variation. Slight changes in the V–O and V–V bonds demonstrate the layered structural stability of $Mg_{0.3}V_2O_5{\cdot}1.1H_2O$ after Mg insertion.

Solid-state magic angle spinning nuclear magnetic resonance (MAS NMR) was performed on the pristine and fully discharged and charged electrodes to provide insights into Mg^{2+} intercalation and the state of structural water in $Mg_{0.3}V_2O_5{\cdot}1.1H_2O$. ^{25}Mg MAS NMR spectroscopy is shown in Figure 5D. For the pristine sample, a weak Mg resonance peak appears at 20.1 ppm, which could be due to a lower Mg-ion content. After a full discharge, two sharp and intense peaks attributable to the existence of different octahedral coordination Mg environment appear at 19.5 and 25.8 ppm, which fully demonstrate Mg^{2+} intercalation into the crystal layers. This result is in agreement with the ^{25}Mg NMR spectra in similar coordination sites reported in the previous reports.[46] After charging, the intensity of the Mg resonance peak becomes weak, and the spectrum resembles that of the pristine sample, indicating Mg^{2+} extraction from the interlayer. The above results provide concrete proof to indicate the reversible Mg^{2+} intercalation within the xerogel structure. To further verify this fact, we performed TEM-EDX element analysis of $Mg_{0.3}V_2O_5{\cdot}1.1H_2O$ nanowires at full charge and discharge states in the tenth cycle, as shown in Figure S13. Both the EDX element mapping images and spectra analysis of the discharged and charged electrode in the tenth cycle indicate the amount of Mg^{2+} inserted or extracted during discharge or charge, respectively. The ^1H NMR spectrum of the pristine sample (black line) shows one main protonic feature located at 6.3 ppm, which is related to the structural water in between the bilayers (Figure 5E). The sharp and intense peak indicates the high migration rate of the water resulting in a large bilayer distance of 11.9 Å.[35] In this state, the structural water in the form of weak hydrogen bonds exists in the lattice with a high degree of freedom, which can be defined as "free" hydrated water.[47] After more Mg^{2+} ions intercalation, the peak at 6.3 ppm gets wider with weaker intensity. Meanwhile, a new broad peak appears at 10.7 ppm (red line), indicating that the water exists in two states in the electrode material. One is the original "free" hydrated water (6.3 ppm), and the other is the water molecule attached to the Mg^{2+} ions (bound water, 10.7 ppm). The intensity attenuation of the peak at 6.3 ppm is because of the increased bonding between Mg^{2+} ions' bonds and the oxygen in water, thereby reducing the amount and mobility of the "free" hydrated water and reducing the bilayer distance from 11.9 to 11.4 Å. After charging, Mg^{2+} ions are extracted from the interlayer. An increase in the intensity of ^1H NMR resonance is observed at 6.3 ppm (blue line) at the expense of 10.7 ppm resonance, confirming the recovery of the amount and mobility of the "free" hydrated water as well as the lattice spacing. These results corroborate the charge "shielding effect" of water, which greatly improves the diffusion kinetics of Mg ions. It needs to be noticed that the water always exists in the lattice in the whole process of charging and

Please cite this article in press as: Xu et al., Vanadium Oxide Pillared by Interlayer Mg^{2+} Ions and Water as Ultralong-Life Cathodes for Magnesium-Ion Batteries, Chem (2019), https://doi.org/10.1016/j.chempr.2019.02.014

discharging, which is different with $Zn_{0.25}V_2O_5 \cdot nH_2O$.[37] We also performed TGA of $Mg_{0.3}V_2O_5 \cdot 1.1H_2O$ nanowires in argon atmosphere after charge and discharge to test the water content, as shown in Figure S14. It can be clearly seen that the two electrodes exhibited similar weight-loss profiles. The weight loss of 9.3% between 100°C and 450°C corresponds to the weight loss of lattice water, which is consistent with the pristine sample shown in Figure S2. Figure S15 shows the ^{13}C NMR spectra of $Mg_{0.3}V_2O_5 \cdot 1.1H_2O$ at a different state. Clearly, the resonances of discharging (red line) and charging (blue line) state are almost the same as that of the pristine sample (black line), demonstrating that the solvent molecule (acetonitrile) does not intercalate into the V_2O_5 bilayers. This differs from the previous report of $V_2O_5 \cdot nH_2O$ xerogel material,[25] which could be because the pre-intercalated Mg^{2+} ions act as "guards" in the interlayers to prevent the insertion of the solvent molecule. Thus, the stability of the crystal structure is guaranteed. Given the above results, the reaction mechanism can be summarized as follows: in the discharge process, Mg^{2+} ions insert into the $Mg_{0.3}V_2O_5 \cdot 1.1H_2O$ bilayer and are shielded by the lattice waters, resulting in magnesiation with small structural variation due to the pillaring effects of the pre-intercalated Mg ions and the water molecules. In the subsequent charge step, Mg^{2+} ions are pulled out of the lattice, and the crystal structure of $Mg_{0.3}V_2O_5 \cdot 1.1H_2O$ is restored to its original state.

Electrochemical Performance of Full MIBs

To further demonstrate the excellent Mg storage performance of $Mg_{0.3}V_2O_5 \cdot 1.1H_2O$, we fabricated full MIBs based on $Mg_{0.3}V_2O_5 \cdot 1.1H_2O$ as the cathode, $Mg(TFSI)_2$-acetonitrile as the electrolyte, and $MgNaTi_3O_7$ as the anode. The $MgNaTi_3O_7$ anode was formed after magnesiation of $Na_2Ti_3O_7$ according to the report of Chen et al.[48] The electrochemical performance of $Na_2Ti_3O_7$ is presented in Figure S16. The mass loading of the anode was twice that of the cathode. Figure 6A shows the schematic of the Mg^{2+} conduction between $Mg_{0.3}V_2O_5 \cdot 1.1H_2O$ and $MgNaTi_3O_7$ during Mg^{2+} insertion and extraction. Both electrode materials were capable of reversibly inserting and extracting Mg ions from their respective skeletal layered structure. During the discharge process, Mg ions were extracted from $MgNaTi_3O_7$ and inserted into $Mg_{0.3}V_2O_5 \cdot 1.1H_2O$. A reversible process takes place during charge. The detailed reaction can be summarized as follows:

$$\text{Cathode: } Mg_{0.3}V_2O_5 \cdot 1.1H_2O + 0.5\ Mg^{2+} + e^- \leftrightarrow Mg_{0.8}V_2O_5 \cdot 1.1H_2O \quad \text{(Equation 2)}$$

$$\text{Anode: } MgNaTi_3O_7 \leftrightarrow Mg_{0.5}NaTi_3O_7 + 0.5\ Mg^{2+} + e^- \quad \text{(Equation 3)}$$

$$\text{Overall: } Mg_{0.3}V_2O_5 \cdot 1.1H_2O + MgNaTi_3O_7 \leftrightarrow Mg_{0.8}V_2O_5 \cdot 1.1H_2O + Mg_{0.5}NaTi_3O_7 \quad \text{(Equation 4)}$$

After being fully charged, our full cell lit up a series of green light-emitting diodes (LEDs) (Figure 6B), implying the practical application potential. The electrochemical performances of the full cell are shown in Figures 6C and 6D. The full cell delivered a discharge capacity of 57 mA h g^{-1} at 100 mA g^{-1} (on the basis of the total mass of the cathode and anode) with an average voltage of 1.50 V (versus Mg^{2+}/Mg) and good reversibility with a capacity retention of 42 mA h g^{-1} after 100 cycles. In addition, a high average Coulombic efficiency of ~97% was achieved during the whole cycles. We performed TEM-EDX elemental analysis of the

Please cite this article in press as: Xu et al., Vanadium Oxide Pillared by Interlayer Mg^{2+} Ions and Water as Ultralong-Life Cathodes for Magnesium-Ion Batteries, Chem (2019), https://doi.org/10.1016/j.chempr.2019.02.014

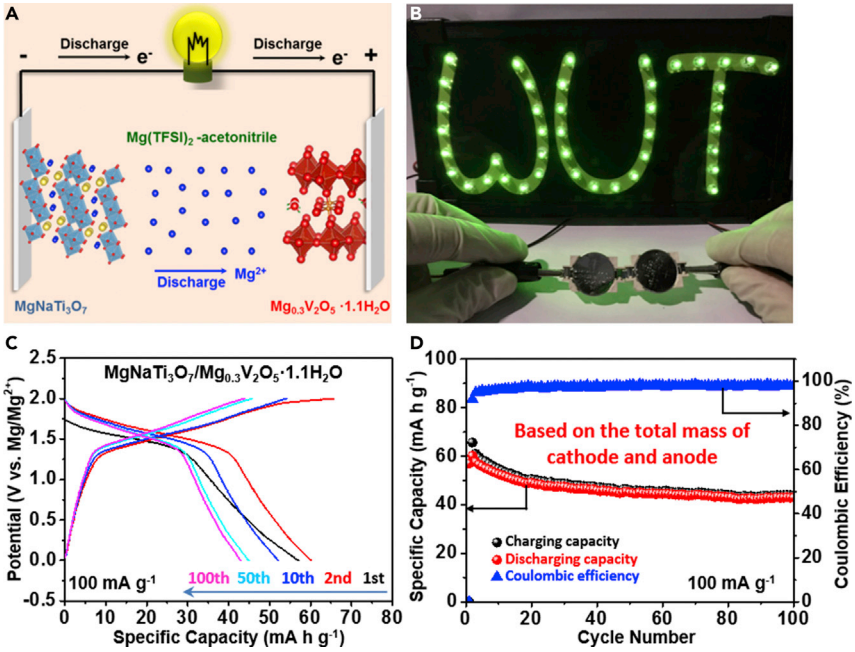

Figure 6. Electrochemical Performance of Full MIBs

(A) Schematic illustration of full cell with $Mg_{0.3}V_2O_5{\cdot}1.1H_2O$ cathode, $Mg(TFSI)_2$-acetonitrile electrolyte, and $MgNaTi_3O_7$ anode.

(B) The lighted LEDs driven by the full MIBs.

(C) Magnesiation-demagnesiation curves.

(D) Cycling performance at 100 mA g^{-1} (the capacity is based on the total mass of the cathode and anode).

discharged and charged $MgNaTi_3O_7$ anode to explore the ion intercalation behavior. In the full charge state, the uniform distributions of Mg, Na, and Ti elements could be clearly seen (Figure S17A). However, in the full discharge state, in addition to Na and Ti, Mg content decreased significantly (Figure S17C). The change in Mg content was also clearly observed in the energy spectrum (Figures S17B and S17D). Meanwhile, both the atomic ratios of Na:Ti were around 1:3 in the two states, indicating that the Na content in $MgNaTi_3O_7$ was unchanged during the charge and discharge process. In addition, Na signal was not observed in the $Mg_{0.3}V_2O_5{\cdot}1.1H_2O$ cathode from the EDX spectrum after full discharge (Figure S18). The results fully demonstrate the Mg^{2+} intercalation instead of Na^+ in the $MgNaTi_3O_7$ anode, which is consistent with the previous report.[48] On the basis of these results, the $Mg_{0.3}V_2O_5{\cdot}1.1H_2O$ exhibits good electrochemical performance in full MIBs, indicating great application potential in energy storage devices and bright future prospects.

DISCUSSION

In summary, we have developed a high-performance cathode material, $Mg_{0.3}V_2O_5{\cdot}1.1H_2O$, for MIBs. The 1D nanostructure endows the short Mg^{2+} diffusion length and large contact area between electrode and electrolyte. From the operando XRD, XANES, and NMR analyses, the water molecules and pre-intercalated Mg^{2+} ions play crucial roles in the electrochemical performance: the water not only expands the lattice spacing of $Mg_{0.3}V_2O_5{\cdot}1.1H_2O$ to allow Mg^{2+} intercalation and deintercalation but also shields the charge of Mg^{2+}, leading to rapid kinetics and good rate performance. The indigenous Mg^{2+} ions ensure high electronic

Please cite this article in press as: Xu et al., Vanadium Oxide Pillared by Interlayer Mg^{2+} Ions and Water as Ultralong-Life Cathodes for Magnesium-Ion Batteries, Chem (2019), https://doi.org/10.1016/j.chempr.2019.02.014

conductivity and act as "pillars" to stabilize the layered structure, thus ensuring long-life cycling stability. Benefiting from the synergistic effect, the $Mg_{0.3}V_2O_5 \cdot 1.1H_2O$ delivers an unprecedented cycling life with capacity retention of 80.0% after 10,000 cycles at a high current density of 2 A g^{-1}. Moreover, the full MIB device ($MgNaTi_3O_7/Mg_{0.3}V_2O_5 \cdot 1.1H_2O$) delivers a reversible discharge capacity of 57 mA h g^{-1} (on the basis of the total mass of the cathode and anode) with good cycling performance, demonstrating a promising application. Therefore, this scalable Mg^{2+} host material brings new opportunities for developing high-performance, low-cost, and extremely safe MIB cathodes to meet the requirements for large-scale storage applications.

EXPERIMENTAL PROCEDURES

Materials Synthesis

$Mg_{0.3}V_2O_5 \cdot 1.1H_2O$ nanowires were prepared via a facile hydrothermal method. First, 3 mmol V_2O_5 (Xiya Reagent, GR, 99.5%) was dissolved in 24 mL deionized water in a beaker and stirred for 30 min in water bath (40°C). Then, 6 mL H_2O_2 (Aladdin, AR, 30.0%) was dropwise added in the solution with continuous magnetic stirring until a homogenous reddish-brown solution was obtained. After that, 1 mmol Mg acetate tetrahydrate (dissolved in 10 mL deionized water) was dropwise added into the above solution with continuous magnetic stirring until a homogenous orange transparent solution was obtained. The mixture was then transferred to a 50 mL Teflon-lined sealed autoclave and maintained at 200°C for 48 h. Afterward, the system was cooled down to room temperature naturally, and the samples were washed with distilled water and ethanol thoroughly three times. Finally, the product was dried at 60°C for 8 h in air, and the green $Mg_{0.3}V_2O_5 \cdot 1.1H_2O$ nanowire powder was obtained. As control experiments, $V_2O_5 \cdot nH_2O$ nanowires were prepared via the same process as $Mg_{0.3}V_2O_5 \cdot 1.1H_2O$ but without Mg acetate tetrahydrate, and $Mg_{0.3}V_2O_5$ was obtained by annealing $Mg_{0.3}V_2O_5 \cdot 1.1H_2O$ at 400°C for 2 h in Ar with a heating rate of 2°C min^{-1}. The $Na_2Ti_3O_7$ materials were prepared according to the report of Chen et al.[48]

Material Characterization

XRD and *in situ* XRD measurements used a D8 Advance X-ray diffractometer with a non-monochromated Cu Kα X-ray source. SEM images were collected with a JEOL-7100F microscope. EDS element mappings were recorded with an Oxford IE250 system. TEM images were recorded by a JEM-2100F STEM/EDS microscope. BET surface areas were measured with a Tristar II 3020 instrument by adsorption of nitrogen at 77 K. TGA was conducted with a STA-449C. XPS measurement was performed with a VG Multi Lab 2000 instrument. ICP-OES (JY/T015-1996) was used to analyze the sample composition quantitatively. An Autolab 302N Probe Station (Lake Shore, TTPX) was used to test the conductivity of the single-nanowire device. XANES was performed to determine the average oxidation state and local structure of the elements in all phases. The XANES measurements were carried out in transmission mode at the beamline 20-BM-B of the APS with a Si (111) monochromator at the Advanced Photon Source of the Argonne National Laboratory. Energy calibration was performed with the first derivative point of the XANES spectrum for the V (K-edge = 5485.70 eV). The XANES and EXAFS data reduction and analysis followed standard methods using the ATHENA software package. Solid-state MAS NMR was performed to test the ^{25}Mg, ^{1}H, and ^{13}C spectrum of the sample on a Varian Inova spectrometer with a 600 MHz magnet.

Measurements of Electrochemical Performance

The electrochemical measurements were carried out by assembling 2016 coin cells in a glove box filled with pure argon. 0.3 M magnesium bis(trifluoromethane sulfonyl)imide ($MgTFSI_2$, Alfa Aesar Co.) in acetonitrile (AN, CH_3CN, Aldrich Co., anhydrous) was used as the electrolyte. Mg electrodes cannot behave reversibly in any conventional non-aqueous solutions because of passivation phenomena. Thus, AC cloth, which is known to be stable in AN-based electrolytes, was used as the counter electrode because of its high surface area, which ensures adequate charge storage via electrical double-layer capacitance to guarantee full charge balance in the Mg intercalation process.[27] The immersion potential of the AC electrode was calculated as 2.4 V versus Mg^{2+}/Mg. The all-phenyl complex (APC) electrolyte and Mg metal were used for testing $Na_2Ti_3O_7$. All active electrodes were made by the mixing of 70 wt % active materials, 20 wt % acetylene black, and 10 wt % polytetrafluoroethylene (PTFE) binder. After drying at 70°C for 12 h, the electrode was dried in a vacuum oven for 4 h at 100°C. The average diameter of the obtained small wafer was about 0.6 cm, and the calculated areal density was around 5 mg cm^{-2}. The glass fiber (GF/D) from Whatman was used as the separator. The galvanostatic discharge-charge tests were carried out on a battery test system (LAND CT2001A). CV and electrochemical impedance spectra (EIS) were tested with an electrochemical workstation (CHI 600e and Autolab PGSTAT 302N).

SUPPLEMENTAL INFORMATION

Supplemental Information can be found with this article online at https://doi.org/10.1016/j.chempr.2019.02.014.

ACKNOWLEDGMENTS

This work was supported by the National Key Research and Development Program of China (2016YFA0202603 and 2016YFA0202601), the National Natural Science Fund for Distinguished Young Scholars (51425204), the National Natural Science Foundation of China (51832004, 51521001, and 51602239), the Programme of Introducing Talents of Discipline to Universities (B17034), the Hubei Provincial Natural Science Foundation of China (2016CFB267), the Yellow Crane Talent (Science & Technology) Program of Wuhan City, the International Science & Technology Cooperation Program of China (2013DFA50840), and the Fundamental Research Funds for the Central Universities (WUT: 2017III009 and 2017III005). The authors are grateful to the X-ray Science Division of the Advanced Photon Source at Argonne National Laboratory for strong support and help.

AUTHOR CONTRIBUTIONS

L.M., Q.A., and Y.X. conceived the study and co-wrote the manuscript. Y.X., X.D., F.X., and S.T. carried out the synthesis and electrochemical evaluation. Q.L., G.Z., Q.W., J. Lu, and J. Li helped with material characterization and manuscript preparation. All authors discussed the results and commented on the manuscript.

DECLARATION OF INTERESTS

The authors declare no competing interests.

Received: December 12, 2018
Revised: January 30, 2019
Accepted: February 14, 2019
Published: March 21, 2019

REFERENCES AND NOTES

1. Goodenough, J.B., and Park, K.S. (2013). The Li-ion rechargeable battery: a perspective. J. Am. Chem. Soc. *135*, 1167–1176.
2. Wanger, T.C. (2011). The lithium future—resources, recycling, and the environment. Conserv. Lett. *4*, 202–206.
3. Jacoby, M. (2013). Safer lithium-ion batteries. Chem. Eng. News *91*, 33–37.
4. Canepa, P., Sai Gautam, G.S., Hannah, D.C., Malik, R., Liu, M., Gallagher, K.G., Persson, K.A., and Ceder, G. (2017). Odyssey of multivalent cathode materials: open questions and future challenges. Chem. Rev. *117*, 4287–4341.
5. Muldoon, J., Bucur, C.B., and Gregory, T. (2014). Quest for nonaqueous multivalent secondary batteries: magnesium and beyond. Chem. Rev. *114*, 11683–11720.
6. Yoo, H.D., Shterenberg, I., Gofer, Y., Gershinsky, G., Pour, N., and Aurbach, D. (2013). Mg rechargeable batteries: an on-going challenge. Energy Environ. Sci. *6*, 2265–2279.
7. Kaveevivitchai, W., and Jacobson, A.J. (2016). High capacity rechargeable magnesium-ion batteries based on a microporous molybdenum–vanadium oxide cathode. Chem. Mater. *28*, 4593–4601.
8. Mukherjee, A., Sa, N., Phillips, P.J., Burrell, A., Vaughey, J., and Klie, R.F. (2017). Direct investigation of Mg intercalation into the orthorhombic V_2O_5 cathode using atomic-resolution transmission electron microscopy. Chem. Mater. *29*, 2218–2226.
9. Ling, C., Banerjee, D., and Matsui, M. (2012). Study of the electrochemical deposition of Mg in the atomic level: why it prefers the non-dendritic morphology. Electrochim. Acta *76*, 270–274.
10. Kim, H., Jeong, G., Kim, Y.U., Kim, J.H., Park, C.M., and Sohn, H.J. (2013). Metallic anodes for next generation secondary batteries. Chem. Soc. Rev. *42*, 9011–9034.
11. Zhang, T., Tao, Z., and Chen, J. (2014). Magnesium–air batteries: from principle to application. Mater. Horiz. *1*, 196–206.
12. Aurbach, D., Lu, Z., Schechter, A., Gofer, Y., Gizbar, H., Turgeman, R., Cohen, Y., Moshkovich, M., and Levi, E. (2000). Prototype systems for rechargeable magnesium batteries. Nature *407*, 724–727.
13. Liu, M., Rong, Z., Malik, R., Canepa, P., Jain, A., Ceder, G., and Persson, K.A. (2015). Spinel compounds as multivalent battery cathodes: a systematic evaluation based on ab initio calculations. Energy Environ. Sci. *8*, 964–974.
14. Sun, X., Duffort, V., Mehdi, B.L., Browning, N.D., and Nazar, L.F. (2016). Investigation of the mechanism of Mg insertion in birnessite in nonaqueous and aqueous rechargeable Mg-ion batteries. Chem. Mater. *28*, 534–542.
15. Gautam, G.S., Sun, X., Duffort, V., Nazar, L.F., and Ceder, G. (2016). Impact of intermediate sites on bulk diffusion barriers: Mg intercalation in $Mg_2Mo_3O_8$. J. Mater. Chem. A *4*, 17643–17648.
16. Rong, Z., Malik, R., Canepa, P., Sai Gautam, G.S., Liu, M., Jain, A., Persson, K., and Ceder, G. (2015). Materials design rules for multivalent ion mobility in intercalation structures. Chem. Mater. *27*, 6016–6021.
17. Tao, Z.L., Xu, L.N., Gou, X.L., Chen, J., and Yuan, H.T. (2004). TiS_2 nanotubes as the cathode materials of Mg-ion batteries. Chem. Commun. *10*, 2080–2081.
18. Liang, Y., Feng, R., Yang, S., Ma, H., Liang, J., and Chen, J. (2011). Rechargeable Mg batteries with graphene-like MoS_2 cathode and ultrasmall Mg nanoparticle anode. Adv. Mater. *23*, 640–643.
19. He, D., Wu, D., Gao, J., Wu, X., Zeng, X., and Ding, W.J. (2015). Flower-like CoS with nanostructures as a new cathode-active material for rechargeable magnesium batteries. J. Power Sources *294*, 643–649.
20. Xiong, F., Fan, Y., Tan, S., Zhou, L., Xu, Y., Pei, C., An, Q., and Mai, L. (2018). Magnesium storage performance and mechanism of CuS cathode. Nano Energy *47*, 210–216.
21. Sutto, T.E., and Duncan, T.T. (2012). Electrochemical and structural characterization of Mg ion intercalation into RuO_2 using an ionic liquid electrolyte. Electrochim. Acta *79*, 170–174.
22. Ling, C., Zhang, R., Arthur, T.S., and Mizuno, F. (2015). How general is the conversion reaction in Mg battery cathode: a case study of the magnesiation of α-MnO_2. Chem. Mater. *27*, 5799–5807.
23. Tepavcevic, S., Liu, Y., Zhou, D., Lai, B., Maser, J., Zuo, X., Chan, H., Král, P., Johnson, C.S., Stamenkovic, V., et al. (2015). Nanostructured layered cathode for rechargeable Mg-ion batteries. ACS Nano *9*, 8194–8205.
24. An, Q., Li, Y., Deog Yoo, H.D., Chen, S., Ru, Q., Mai, L., and Yao, Y. (2015). Graphene decorated vanadium oxide nanowire aerogel for long-cycle-life magnesium battery cathodes. Nano Energy *18*, 265–272.
25. Sa, N., Kinnibrugh, T.L., Wang, H., Sai Gautam, G., Chapman, K.W., Vaughey, J.T., Key, B., Fister, T.T., Freeland, J.W., Proffit, D.L., et al. (2016). Structural evolution of reversible Mg insertion into a bilayer structure of $V_2O_5{\cdot}nH_2O$ xerogel material. Chem. Mater. *28*, 2962–2969.
26. Gershinsky, G., Yoo, H.D., Gofer, Y., and Aurbach, D. (2013). Electrochemical and spectroscopic analysis of Mg^{2+} intercalation into thin film electrodes of layered oxides: V_2O_5 and MoO_3. Langmuir *29*, 10964–10972.
27. Andrews, J.L., Mukherjee, A., Yoo, H.D., Parija, A., Marley, P.M., Fakra, S., Prendergast, D., Cabana, J., Klie, R.F., and Banerjee, S. (2018). Reversible Mg-ion insertion in a metastable one-dimensional polymorph of V_2O_5. Chem *4*, 564–585.
28. Orikasa, Y., Masese, T., Koyama, Y., Mori, T., Hattori, M., Yamamoto, K., Okado, T., Huang, Z.D., Minato, T., Tassel, C., et al. (2014). High energy density rechargeable magnesium battery using earth-abundant and non-toxic elements. Sci. Rep. *4*, 5622.
29. Huang, Z.D., Masese, T., Orikasa, Y., Mori, T., Minato, T., Tassel, C., Kobayashi, Y., Kageyama, H., and Uchimoto, Y. (2014). $MgFePO_4F$ as a feasible cathode material for magnesium batteries. J. Mater. Chem. A *2*, 11578–11582.
30. Novák, P., Imhof, R., and Haas, O. (1999). Magnesium insertion electrodes for rechargeable nonaqueous batteries — a competitive alternative to lithium? Electrochim. Acta *45*, 351–367.
31. Yin, J., Pelliccione, C.J., Lee, S.H., Takeuchi, E.S., Takeuchi, K.J., and Marschilok, A.C. (2016). Communication—sol-gel synthesized magnesium vanadium oxide, $Mg_xV_2O_5{\cdot}nH_2O$: the role of structural Mg^{2+} on battery performance. J. Electrochem. Soc. *163*, A1941–A1943.
32. Zhang, Q., Takeuchi, E.S., Takeuchi, K.J., and Marschilok, A.C. (2015). High energy density electrode materials for rechargeable magnesium batteries. ECS Trans. *66*, 171–181.
33. Sai Gautam, G.G., Canepa, P., Richards, W.D., Malik, R., and Ceder, G. (2016). Role of structural H_2O in intercalation electrodes: the case of Mg in nanocrystalline xerogel-V_2O_5. Nano Lett. *16*, 2426–2431.
34. Kristoffersen, H.H., and Metiu, H. (2016). Structure of $V_2O_5{\cdot}nH_2O$ xerogels. J. Phys. Chem. C *120*, 3986–3992.
35. Yan, M., He, P., Chen, Y., Wang, S., Wei, Q., Zhao, K., Xu, X., An, Q., Shuang, Y., Shao, Y., et al. (2017). Water-lubricated intercalation in $V_2O_5{\cdot}nH_2O$ for high-capacity and high-rate aqueous rechargeable zinc batteries. Adv. Mater. *30*, 1703725.
36. Xu, K., Hu, S., Wu, C., Lin, C., Lu, X., Peng, L., Yang, J., and Xie, Y. (2012). Highly entangled $K_{0.5}V_2O_5$ superlong nanobelt membranes for flexible nonvolatile memory devices. J. Mater. Chem. *22*, 18214–18220.
37. Kundu, D., Adams, B.D., Duffort, V., Vajargah, S.H., and Nazar, L.F. (2016). A high-capacity and long-life aqueous rechargeable zinc battery using a metal oxide intercalation cathode. Nat. Energy *1*, 16119.
38. He, P., Zhang, G., Liao, X., Yan, M., Xu, X., An, Q., Liu, J., and Mai, L. (2018). Sodium ion stabilized vanadium oxide nanowire cathode for high-performance zinc-ion batteries. Adv. Energy Mater. *8*, 1702463.
39. Shterenberg, I., Salama, M., Gofer, Y., Levi, E., and Aurbach, D. (2014). The challenge of developing rechargeable magnesium batteries. MRS Bull. *39*, 453–460.
40. Qu, Q., Liu, L., Wu, Y., and Holze, R. (2013). Electrochemical behavior of V_2O_5 center dot 0.6H(2)O nanoribbons in neutral aqueous electrolyte solution. Electrochim. Acta *96*, 8–12.
41. Wei, Q., Liu, J., Feng, W., Sheng, J., Tian, X., He, L., An, Q., and Mai, L. (2015). Hydrated vanadium pentoxide with superior sodium storage capacity. J. Mater. Chem. A *3*, 8070–8075.
42. Zhang, G., Xiong, T., Yan, M., He, L., Liao, X., He, C., Yin, C., Zhang, H., and Mai, L. (2018). α-MoO_{3-x} by plasma etching with improved

capacity and stabilized structure for lithium storage. Nano Energy *49*, 555–563.

43. Giorgetti, M., Passerini, S., Smyrl, W.H., Mukerjee, S., Yang, X., and McBreen, J. (1999). In situ X-ray absorption spectroscopy characterization of V_2O_5 xerogel cathodes upon lithium intercalation. J. Electrochem. Soc. *146*, 2387–2392.

44. Liu, Q., Li, Z.F., Liu, Y., Zhang, H., Ren, Y., Sun, C.J., Lu, W., Zhou, Y., Stanciu, L., Stach, E.A., et al. (2015). Graphene-modified nanostructured vanadium pentoxide hybrids with extraordinary electrochemical performance for Li-ion batteries. Nat. Commun. *6*, 6127.

45. Stallworth, P.E., Kostov, S., denBoer, M.L., Greenbaum, S.G., and Lampe-Onnerud, C. (1998). X-ray absorption and magnetic resonance spectroscopic studies of $Li_xV_6O_{13}$. J. Appl. Phys. *83*, 1247–1255.

46. Pallister, P.J., Moudrakovski, I.L., and Ripmeester, J.A. (2009). Mg-25 ultra-high field solid state NMR spectroscopy and first principles calculations of magnesium compounds. Phys. Chem. Chem. Phys. *11*, 11487–11500.

47. Han, J.H., Lee, K.W., Jeon, G.W., Lee, C.E., Park, W.K., and Choi, E.H. (2015). 1H Nuclear magnetic resonance study of hydrated water dynamics in perfluorosulfonic acid ionomer nafion. Appl. Phys. Lett. *106*, 023104.

48. Chen, C., Wang, J., Zhao, Q., Wang, Y., and Chen, J. (2016). Layered $Na_2Ti_3O_7$/$MgNaTi_3O_7$/$Mg_{0.5}NaTi_3O_7$ nanoribbons as high-performance anode of rechargeable Mg-ion batteries. ACS Energy Lett. *1*, 1165–1172.